Detailed microkinetics for the oxidation of exhaust gas emissions through automated mechanism generation

Bjarne Kreitz,[*,†,‡] Patrick Lott,[‡] Jongyoon Bae,[†] Katrín Blöndal,[†] Sofia Angeli,[‡] Zachary W. Ulissi,[¶] Felix Studt,[§,‡] C. Franklin Goldsmith,[†] and Olaf Deutschmann[*,‡]

†School of Engineering, Brown University, Providence, RI 02912, USA

‡Institute for Chemical Technology and Polymer Chemistry, Karlsruhe Institute of Technology, 76131 Karlsruhe, Germany

¶Department of Chemical Engineering, Carnegie Mellon University, Pittsburgh, PA 15213, USA

§Institute of Catalysis Research and Technology, Karlsruhe Institute of Technology, 76344 Eggenstein-Leopoldshafen, Germany

E-mail: bjarne_kreitz@brown.edu(B.K.); deutschmann@kit.edu(O.D.)

Phone: +1 401 263-1480 (B.K.); +49 721 608-43064 (O.D.)

Abstract

Emissions from vehicles contain a variety of pollutants that must be either oxidized or reduced efficiently in the catalytic converter. Improvements to the catalyst require knowledge of the microkinetics, but the complexity of the exhaust gas mixture makes it challenging to identify the reaction network. This complexity was tackled by using the "Reaction Mechanism Generator" (RMG) to automatically generate microkinetic

1

models for the oxidation of combustion byproducts from stoichiometric gasoline direct injection engines on Pt(111). The possibilities and the limitations encountered during the generation procedure are discussed in detail. A combination of first-principles-based mechanism construction and top-down parameter refinement allows to describe experimental results obtained by kinetic testing of a Pt/Al_2O_3 monolith under stoichiometric conditions. The study can serve as a blueprint for the usage of RMG for other challenging heterogeneously catalyzed reactions.

Introduction

The abatement of emissions from internal combustion engines to reduce the effect on the environment and to meet more stringent government regulations necessitates further improvement of catalytic converters.[1,2] Pt is usually the active metal for oxidation in the three-way catalytic converters for stoichiometric gasoline direct injection (S-GDI) engines. Improvement of the converters through tailoring of the catalyst – as well as overcoming current hurdles, i.e. cold start emissions[1] – requires a deeper understanding of the mechanism and the microkinetics of all elementary steps on the catalyst surface. However, the exhaust gas contains more than 100 species,[3,4] such as $CH_4, CO, H_2, C_2H_4, C_2H_6, C_3H_6$, and NO, which makes mechanism development a daunting task.

Microkinetic models for the oxidation of these pollutants over Pt can be divided into two categories: first-principles-based[5–8] and semi-empirical.[9–15] The semi-empirical models are developed for complex reaction mixtures, including e.g. propene[10,11,15] and usually achieve a reasonably accurate postdictive prediction of the experimental results after tuning various activation energies.[9–12,15] The first-principles-based microkinetic models are constructed by extensive density functional theory (DFT) calculations and focus mostly on the oxidation of CO or CH_4 on Pt(111) and Pt(211),[5,7,8,16–19] but they fail to predict experimental results. To the best of our knowledge, the only first-principles-based model for a larger molecule was constructed by Peela et al.,[6] for C_2H_6 oxidation over Pt(111) under lean-burn conditions using a combination of DFT and Brønsted-Evans-Polanyi (BEP) relations. Yet, no first-principles-based microkinetic models are available that thoroughly explore all the pathways for the oxidation of the complicated exhaust gas mixtures from stoichiometric combustion conditions over the Pt catalyst and also quantitatively predict experimental results.

This scarcity of detailed microkinetic mechanisms is due to the intricate complexity of the reaction networks, because all the possible pathways and intermediates from the vast chemical reaction space must be considered.[20] On a first-principles-basis, it means performing numerous expensive DFT calculations, which becomes impractical if the mechanisms get too large. Using automated mechanism generation software, such as the "Reaction Mechanism Generator" (RMG)[21–23] instead of building the microkinetics based on chemical intuition, reduces personal bias and accelerates the procedure of the mechanism construction. RMG

is a well-established open-source tool to automatically build comprehensive gas-phase mechanisms for combustion or pyrolysis reactions.[24–28] However, RMG has only recently been used for heterogeneously catalyzed reactions.[29–32] The publications on the heterogeneous catalysis branch of RMG are focused on demonstrating new features rather than developing a microkinetic model suitable to describe experimental results. Blöndal et al.[30] developed a thermochemistry database for adsorbates on the Pt(111) surface and showed that RMG could be used to generate mechanisms for coupled homogeneous/heterogeneous reactions for methane oxidation. In order to estimate the thermochemistry on all other metals, Mazeau et al.[31] have implemented linear scaling relations[33] in RMG. Recently, some of the authors demonstrated the capability of RMG to generate mechanisms for the CO_2 methanation on Ni(111)[32,34] while considering the correlated uncertainties in the energetic parameters.[32] In the study of Kreitz et al.,[32] the generated mechanism for the methanation on Ni(111) was in good agreement with temperature-scanning experiments from a Ni/SiO_2 catalyst.[35] RMG has so far only been employed to investigate the chemistry of small molecules on heterogeneous catalysts, and little is known about how well it performs for the C_2 chemistry and beyond.

When a microkinetic mechanism is developed for a specific system, only the final results are presented in the manuscript. The iterative procedure that was used to construct and validate the mechanism is typically neglected. Accordingly, the aim of this study is twofold. First, RMG is used to develop a microkinetic model for the oxidation of the complicated exhaust gas mixtures from S-GDI engines on Pt(111) under stoichiometric conditions, and this mechanism is compared with experiments through mean-field microkinetic modeling. Second, the present work provides a detailed description of how the final mechanism was constructed, so as to provide a template for microkinetic mechanism construction using open-source software, such as RMG. We show the current capabilities but also the limitations of RMG in discovering mechanisms for heterogeneously catalyzed reactions and highlight the research directions for further improvement. An iterative hierarchical framework is applied to refine the thermochemistry of important intermediates with DFT and adjust the predicted reaction barriers of rate-determining steps to match the experimental results. We use a pre-trained machine learning potential from the Open Catalyst Project[36] to accelerate the DFT calculations by obtaining converged initial structures at very low cost, which are further refined by DFT calculations. Through this combined bottom-up/top-down approach, it was possible to automatically build a microkinetic model that can accurately describe the experiments and provide insights into the role of the Pt(111) facet for the emission oxidation chemistry.

Materials and Methods

Material preparation and characterization

Catalyst preparation A $3\,wt\%$ Pt/Al_2O_3 catalyst powder was prepared by incipient wetness impregnation using commercial γ-Al_2O_3 (Puralox, SASOL) that was calcined for $5\,h$ at $700\,°C$ as support material and $(NH_3)_4Pt(NO_3)_2$ (VWR, purity $> 99.9\,\%$) as a precursor that is dissolved in purified water (ROTIPURAN® Ultra, Carl Roth GmbH + Co. KG). After

2 h of drying at 80 °C and 5 h of calcination at 550 °C in static air, the received catalyst powder was coated onto a monolithic honeycomb cordierite substrate (Corning) exhibiting a cell density of 400 cpsi, a wall thickness of 4.50 mil, a length of 5.00 cm and a diameter of 2.54 cm. For this, an aqueous slurry was prepared and applied onto the substrate through dip-coating, analogous to the procedure described by Karinshak et al.[37]

Catalyst characterization After degassing the catalyst powder for 2 h at 300 °C, N_2 physisorption measurements at −196 °C using a BELSORP mini II analyzer (Microtrac-BEL) were used to determine the surface area and pore size according to the Brunauer-Emmet-Teller (BET) method, which amounts to $189\,m^2\,g^{-1}$ and 9.9 nm, respectively. The noble metal dispersion was determined by means of CO chemisorption and temperature-programmed desorption (TPD) in a continuous-flow reactor at atmospheric conditions as described in earlier publications[9,38] assuming a CO:Pt adsorption stoichiometry of 1:1.[39]

Catalyst testing

Setup Catalytic activity measurements of the monolithic samples were conducted in an in-house developed laboratory catalyst testing bench that was already described in a previous publication,[40] optimized for three-way catalysis during the present work. The monolithic catalyst sample was mounted in a cylindrical quartz glass sample holder and placed in a plug-flow quartz glass tubular reactor. A customized electrical furnace (HTM Reetz GmbH) surrounding the entire reactor heated the reaction gases and ensured a linear temperature profile in the sample zone. Two type N thermocouples (d = 1 mm) connected to Eurotherm controllers (Schneider Electric Systems Germany GmbH) were placed approximately 1 mm up- and downstream of the sample to ensure accurate temperature control and monitoring. Gaseous species were dosed via mass flow controllers (Bronkhorst Deutschland Nord GmbH) and a controlled evaporation mixing system (Bronkhorst Deutschland Nord GmbH) provided steam. Finally, a MultiGas 2030 Fourier-transform infrared (FTIR) spectrometer (MKS Instruments) and a Magnos 16 oxygen analyzer (Hartmann & Braun/ABB) were used for the continuous end-of-pipe analysis of the effluent gas stream. In addition, two wideband lambda sensors (LSU 4.9, Bosch) up- and downstream the reactor allowed probing of the oxygen content. Setup control and simultaneous data collection of all relevant setup parameters (temperature, gas flow, gas species) from the different devices was realized by exploiting an in-house developed LabView-based control software.

Experimental procedure The monolith catalyst was de-greened according to common procedures[41] at 700 °C in 10 % O_2, 5 % H_2O, 5 % CO_2 in N_2 with a GHSV of $30\,000\,h^{-1}$ for 4 h before conducting transient activity tests. These catalytic tests comprised a series of consecutive light-out runs with a temperature ramp of $2\,K\,min^{-1}$ as depicted schematically in Figure S1. The gas mixtures were systematically varied as summarized in Table 1 to uncover the impact of different gas species on the catalytic activity. Note that the oxygen concentrations required for achieving $\lambda = 1$ were calculated with the λ-equation (Equation (1)),[42–44] where y are the mole fractions. The stoichiometry of the feed gas was additionally verified

via the setup's upstream lambda sensor.

$$\lambda = \frac{2y_{O_2} + y_{NO} + 2y_{NO_2} + y_{CO} + 2y_{CO_2} + y_{H_2O}}{2y_{CO} + y_{H_2} + 3ny_{C_nH_{2n}} + (3n+1)\,y_{C_nH_{2n+2}} + 2y_{CO_2} + y_{H_2O}} \tag{1}$$

Table 1: Summary of the conducted experiments for the conversion of representative model mixtures for exhaust gas compositions (without NO) from S-GDI engines on a Pt/Al_2O_3 monolith adapted from Ref. 45. N_2 was used as a balance gas.

#	O_2	CO_2 (%)	H_2O	CH_4	H_2	CO (ppm)	C_2H_4	C_2H_6
1	0.6	-	-	3000	-	-	-	-
2	0.25	-	-	-	-	5000	-	-
3	0.6	12	12	3000	-	-	-	-
4	0.9335	12	12	3000	1670	5000	-	-
5	1.031	12	12	3000	1670	5000	325	-
6	1.1085	12	12	3000	1670	5000	-	500
7	1.206	12	12	3000	1670	5000	325	500

Theoretical Methods

Electronic Structure Theory   DFT calculations were performed with QuantumEspresso[46,47] using projector-augmented wave pseudopotentials[48] and ASE[49] to interface with the calculator. Exchange-correlation was treated with the BEEF-vdW functional.[50] The lattice constant for the Pt(111) unit cell was optimized using a Monkhorst-Pack mesh of $(25\times25\times25)$ with a cutoff energy of 70 Ry. The optimized lattice constant is $a = 4.00$ Å in agreement with the experimental value.[51] Electronic structures of adsorbates were calculated in a (3×3) supercell at $1/9^{th}$ of a monolayer (ML) coverage with 8.5 Å of vacuum above and below the slab. The Brillouin zone was sampled with a $(5\times5\times1)$ k-point grid. Electron orbitals were smeared with the Mazari-Vanderbilt method and an electron temperature of 0.02 Ry. Adsorbates were first relaxed on a completely frozen metal slab with a cutoff of 50 Ry until all forces were converged to at least $2.5\,\text{meV Å}^{-1}$. These relaxed structures were then further optimized together with the two top layers of the slab at otherwise identical settings. Single-point energies were calculated for an energy cutoff of 60 Ry. Gas-phase molecules were computed in a box of $10\,\text{Å}^3$ at the Γ-point using Gaussian smearing with a low broadening of 0.005 Ry. The vibrational analysis was performed with ASE. In the case of imaginary vibrational modes, the structure was further optimized until forces were below $1\,\text{meV Å}^{-1}$. If imaginary modes persisted, these were set to $12\,\text{cm}^{-1}$ similar to Ref. 52.

Initial structures of the predicted adsorbates were generated by using the machine learning potential (MLP) from the OpenCatalystProject (OCP).[36] The GemNet-dT OCP calculator trained on all splits was used. Gas-phase molecules were manually placed in a variety of different configurations on the Pt slab and optimized with the MLP until forces were converged below $2.5\,\text{meV Å}^{-1}$. All unique structures obtained from the pre-screening with the

MLP were further relaxed with DFT to identify the most stable adsorbate configuration. This procedure resulted in a speed-up of the subsequent electronic structure calculations with approximately 30 % fewer DFT calls to achieve convergence.[53]

We followed the approach outlined by Blöndal et al.[30] to determine the reference enthalpy of formation $\Delta_f H$, entropy S and the temperature-dependent heat capacity c_p of the adsorbates using the Active Thermochemical Tables (ATcT).[54,55] The vibrational modes were converted to partition functions applying the harmonic oscillator approximation using standard statistical routines previously used in our group.[30] In the case of two or more vibrational frequencies below $100\,\mathrm{cm}^{-1}$ for an adsorbate, the two lowest vibrational modes corresponding to frustrated translation were replaced with partition functions of a 2D gas model, while the remaining modes are treated as harmonic oscillators.

Automated Mechanism Generation Mechanisms for the oxidation of the combustion engine emissions on Pt(111) were generated automatically with RMG.[21–23] RMG can construct arbitrarily large microkinetic models by considering all the possible chemistry significantly faster and more consistently than done by humans. The software achieves this by using templates that convert chemical graphs from educts to products and precompiled *ab-initio* based databases as well as estimation routines. The basic functionality of RMG is described in great detail in Ref. 21,22 and the heterogeneous catalysis features in Ref. 29. Hence, only a brief description of the essentials of RMG important for this work is given below.

Energetic parameters, such as heat of formation of adsorbates and activation energies of reactions, are determined either from precompiled databases or estimated via approximate routines. Thence, RMG can consider all the possible yet *a priori* unknown species and pathways in the mechanism generation procedure. RMG filters out the important intermediates and reactions from the discovered chemistry by employing a rate-based algorithm.[56] Initially, RMG starts with input species provided in the *core*, which are typically, but not limited to, the reactants. The core contains all the chemistry that is important at the specified conditions. For the first iteration, RMG predicts all possible reactions between the core species and places them in the *edge*. The system is then integrated in a reactor simulation, and all reaction rates are evaluated. RMG keeps track of the characteristic rate of reaction R_char computed according to Equation (2), considering production rates R_j of all species j in the core during the simulation to determine whether a species is kinetically significant.

$$R_\mathrm{char} = \sqrt{\sum_{j}^{N_\mathrm{core}} R_j^2} \tag{2}$$

Species j is deemed kinetically relevant and accordingly moved to the core, if its rate of production exceeds a threshold value, $R_j > \epsilon_\mathrm{core} R_\mathrm{char}$, where ϵ_core is a tolerance defined by the user. Afterward, RMG reacts the core together anew, predicts all possible pathways and species, and starts again with the simulation. This procedure continues until RMG reaches a user-defined stopping criterion without discovering kinetically relevant reactions. Finally, the

core contains all relevant pathways and is further used for microkinetic modeling, whereas the model edge contains all the chemistry that has been considered but is deemed unimportant. We used the characteristic rate ratio, the ratio between the characteristic rate of the first iteration step and the n-th iteration (`TerminationRateRatio`) as termination criterion. If this ratio drops below a threshold value, the iteration procedure is terminated. This criterion makes the comparison of generated mechanisms for different mixtures comparable due to the several reactants that are simultaneously converted.

The thermophysical properties of adsorbates are determined from a reference database for Pt(111),[30] which implies that these properties are at the accuracy of the BEEF-vdW DFT level, assuming a harmonic oscillator model for the adsorbate partition function. In case a species is not in the database, RMG estimates its thermochemistry from the gas-phase molecule, which itself is either from a database or estimated via group additivity, and then applies an adsorption correction.[29,57] RMG can estimate reaction kinetics based on training reactions, which are used to populate nodes in a tree-structured database or rate rules such as Brønsted-Evans-Polanyi (BEP)[58]

$$E_{\mathrm{a}} = E_{\mathrm{a}}^0 + \alpha \Delta H_{\mathrm{rxn}} \tag{3}$$

where α is the slope, E_{a}^0 is the intercept, and ΔH_{rxn} is the heat of the reaction. BEP relations have been proven to be universal for surface reaction mechanisms in a variety of studies and predictions are suitably accurate.[6,59–61] Therefore, the usage of training reactions was turned off, and we relied exclusively on BEP relations for the reaction families to estimate the reaction kinetics of all elementary steps, similar to the procedure reported by Kreitz et al.[32] Parameters for the BEP relations are based on values reported in the literature[32,62–67] and are summarized in Table S2. In the generated mechanisms, we provide only the Arrhenius parameters for the forward rate constant; the reverse rate constant is computed from the equilibrium constant, which is determined from the thermochemistry of the adsorbates. As a consequence, all generated microkinetic models are always thermodynamically consistent, as demonstrated in Ref. 32.

Mechanisms were generated for exhaust gas mixtures with different levels of complexity: only CH_4, O_2 (exp. #1 in Table 1), plus CO_2, H_2O (#3), plus CO, H_2 (#4), and plus C_2H_4, C_2H_6 (#7) at atmospheric pressure and an array of temperatures using RMG's build-in ranged reactor feature.[22] We neglect NO in the present study, a major pollutant in the exhaust from S-GDI engines, because RMG's databases for nitrogen chemistry are scarcely populated. This absence of reliable thermophysical properties and kinetic parameters results in flawed predictions; improvements to RMG's nitrogen capabilities is under active development. The settings applied in the generation procedure are summarized in Table S1 and input files are provided in Ref 68. For the temperatures and pressures considered for this study, gas-phase reactions are expected to be negligible;[30] accordingly, although RMG can explore gas-phase reactions in parallel with surface reactions, we choose to turn off this feature to reduce computational overhead. This assumption was confirmed by a coupled homogeneous/heterogeneous reaction mechanisms generation test.

Reactor Modeling and Mechanism Evaluation The experimental setup with the monolithic reactor was modeled as a plug-flow reactor within the Cantera[69] framework employing a chain of 100 continuously stirred-tank reactors (CSTR). The transient light-out experiments were approximated by computing the steady-state solution of the PFR at various temperature increments. All model parameters are summarized in Table S3. Recently, the feature for the inclusion of coverage-dependent thermochemistry was added to Cantera (see SI). A second-order polynomial is used to describe the coverage dependence of the heat of formation $\Delta_f H_i$ of adsorbate i as a function of the coverage Θ of species j

$$\Delta_f H_i = \Delta_f H_i^{\text{ref}} + \sum_j a_{i,j} \Theta_j + \sum_j b_{i,j} \Theta_j^2 \tag{4}$$

where a and b are parameters for the coverage relation fitted to DFT results and summarized in Table S8. The effect of coverage on entropy and heat capacity has been neglected due to anticipated minor contributions. Reaction path analysis was performed with Cantera.[69] The relative importance of various elementary steps was quantified with the degree of rate control (DRC) according to Equation (6) with respect to the consumption rate r_j of reactant j.[70–72] A thermodynamic sensitivity analysis for the free energy of formation was conducted, analogous with, but not equivalent to the thermodynamic DRC[71] (see SI for an explanation of the difference). The definition of the thermodynamic sensitivity coefficient S_{thermo} is given in Equation (5) and of the DRC X_{RC} in Equation (6).

$$S_{\text{thermo}} = \frac{1}{r_j} \left(\frac{\partial r_j}{\partial \left(\frac{-\Delta_f G_k}{RT} \right)} \right) \tag{5}$$

$$X_{\text{RC}} = \frac{k_i}{r_j} \left(\frac{\partial r_j}{\partial k_i} \right) \tag{6}$$

Forward and reverse rate constant k_i of elementary reaction i are perturbed by 1% to ensure thermodynamic consistency when determining the DRC (X_{RC}). The Gibbs free energy of formation $\Delta_f G_k$ of adsorbate k is adjusted by $0.1\,\text{kJ}\,\text{mol}^{-1}$ for the thermodynamic sensitivity analysis.

Results and Discussion

Kinetic activity experiments

Figure 1 shows a summary of the kinetic activity test with the Pt/Al_2O_3 monolith under different stoichiometric gas mixtures. The conversion of CH_4 in the CO_2 and H_2O atmosphere encountered in stoichiometric combustion conditions is displayed in Figure 1a. CH_4 conversion begins at $400\,°C$, reaches 50% conversion at $508\,°C$ (T_{50}) and full conversion is obtained beyond $550\,°C$. Neither CO_2 nor H_2O has any observable effect on the CH_4 oxidation rate, in contrast to experiments on Pd, where H_2O strongly inhibits the conversion.[73,74]

It also shows that reforming pathways do not occur in the oxidative environment. Figure 1b displays the light-out curve for CO. CO is oxidized at lower temperatures, with a start at 150 °C. The addition of CO and H_2 to the CH_4 mixture decreases the onset temperature for CH_4 oxidation and the T_{50} by 50 K, as seen in Figure 1c. Similarly, the T_{50} for CO is decreased by 70 K when H_2 is added, also reported by Gänzler et al.[75] Although the O_2 concentration is increased in the gas phase, the Pt crystals are locally exposed to a more reductive atmosphere (H_2, CO), which can alter catalyst morphology and oxidation state[76,77] that affect the activity.

Moving on to the influence of larger hydrocarbons, the addition of C_2H_4 (Figure 1d) accelerates the conversion of CH_4, whereas the addition of C_2H_6 (Figure 1e) does not have an effect on methane's light-off temperature. However, the T_{50} for CO is retarded in both cases. C_2H_4 has almost an identical conversion profile as CO. C_2H_6 has a T_{50} of 385 °C, which is significantly lower than CH_4, because the activation of the C−H bond in C_2H_6 requires substantially less energy than CH_4.[65] Figure 1f shows the light-out experiment with all components, which does not differ from the experiments in Figure 1d,e. Finally, it should be kept in mind that these conversion profiles would be vastly different in the presence of NO, due to its oxidizing potential.[45] The investigation of the effect of NO is beyond the scope of the present study.
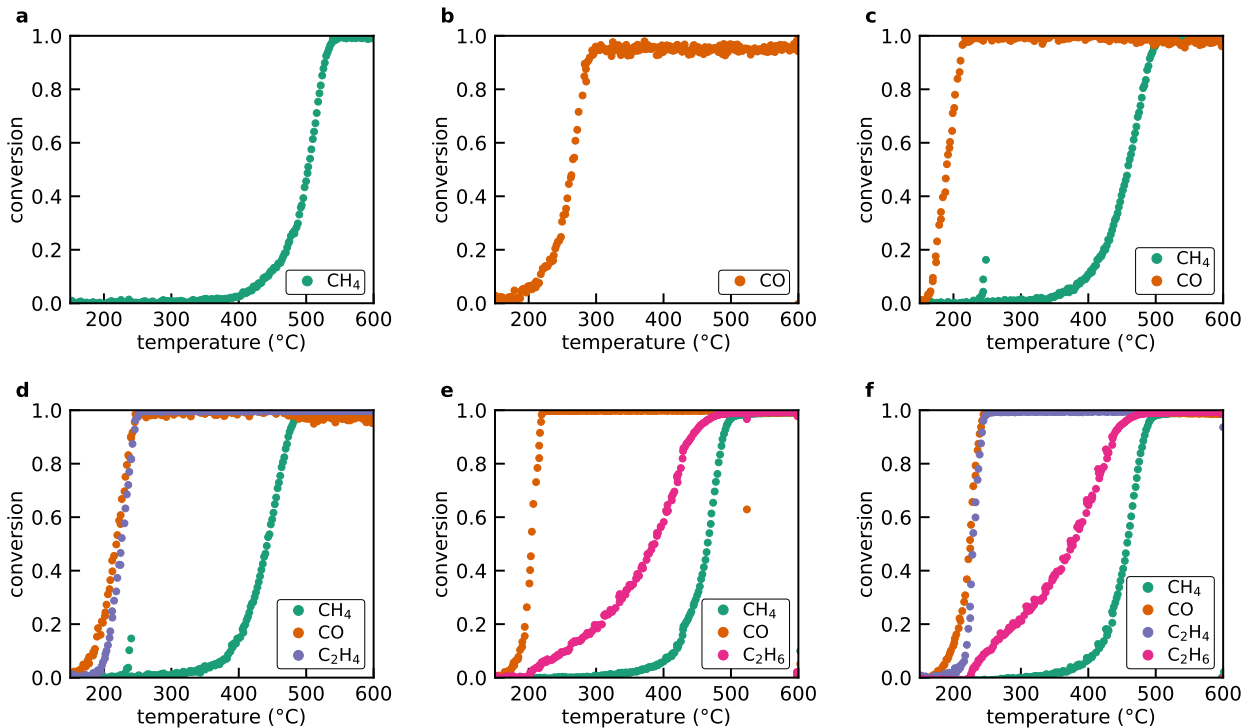

Figure 1: Kinetic activity test results for different stoichiometric gas mixtures (Table 1). a) CH_4, O_2, CO_2 and H_2O (experiment #3), b) CO oxidation (#2), c) CH_4, O_2, CO_2, H_2O, H_2, and CO (base case) (#4), d) base case + C_2H_4 (#5), e) base case + C_2H_6 (#6), and f) base case + C_2H_4 + C_2H_6 (#7).

Initial Discovered Mechanisms

Table 2 summarizes the kinetically relevant subset of the considered species and reactions by RMG for the different reaction mixtures. The mechanism for the oxidation of pure CH_4 contains 41 species and 128 reactions, which RMG's rate-based algorithm deems to be important. Interestingly, even for this simple case, a full 50% of the discovered reactions in the core mechanism are abstraction reactions. These reactions include the abstraction of larger moieties and are not limited to the abstraction of H atoms by O^* or OH^* in oxidative dehydrogenation reactions typically considered for the oxidation chemistry.[63] The addition of CO_2 and H_2O as well as H_2 and CO actually leads to smaller mechanisms, which is a consequence of the rate-based algorithm and the termination criterion. In the initial step of the mechanism generation for the oxidation of the pure CH_4, the reaction rates are quite low, and consequently, so is the threshold for the termination criterion. In contrast, the addition of CO_2 and H_2O leads to higher initial reaction rates due to adsorption of CO_2 and H_2O, which leads to a higher characteristic rate, and thus the threshold for the termination is higher. This result illustrates nicely that the discovered mechanism depends on the initial reactant and concentration as well as the termination criteria.

Table 2: Summary of the discovered mechanisms by RMG for different exhaust gas mixtures for stoichiometric combustion conditions. N_2 is used as a balance.

Experiment	Core		Core + Edge		Time
	Species	Reactions	Species	Reactions	
0.6% O_2 0.3% CH_4 (#1)	41	128	184	484	08:28
+ 12% CO_2, 12% H_2O (#3)	25	43	55	100	01:53
+ 0.167% H_2, 0.5% CO (#4)	25	43	55	100	01:31
+ 0.0325% C_2H_4, 0.05% C_2H_6 (#7)	56	334	578	1651	13:01

When the C_2 chemistry is considered, the mechanism generator shows its full potential. The number of intermediates is more than doubled, and the number of reactions increases by nearly one order of magnitude. The total number of species and reactions considered is even larger, with factors of 11 and 16, respectively. We wish to highlight that it takes a mere 13 min to generate a fully parameterized microkinetic model for a complicated reaction system on a single core with a typical office notebook (Lenovo ThinkPad E490, IntelCore I7).

Microkinetic modeling

Figure 2a presents the results of the simulation with the generated mechanisms for the oxidation of CO, H_2, CH_4 and C_2H_4. Comparing the simulation with the experimental results shows that the generated model predicts a significantly lower activity than the experiments. The simulated conversion of CO sets in at temperatures of 390 °C, whereas in the experiment CO is already fully converted below 220 °C. A similar shift in temperature is observed for the CH_4 conversion profile. Moreover, the model predicts that C_2H_4 is converted after CH_4, in obvious disagreement with experiments[45] as well as theoretical studies on the activation of

the C−H bond in alkanes.[65] The coverage profile in Figure 2b reveals the reason for the shift to higher temperatures. *CO effectively poisons the entire surface at temperatures below 400 °C, and *O similarly saturates the surface from 400 °C to temperatures beyond 700 °C, since both *CO and O* bind strongly to the Pt(111) surface.[66,78] The conversion of CO and CH$_4$ begins when temperatures are high enough for *CO and *O to desorb, thereby providing the necessary vacant sites. The reactions are almost instantaneous when the species start to desorb, as shown by the steep conversion slope and similar coverage profiles.
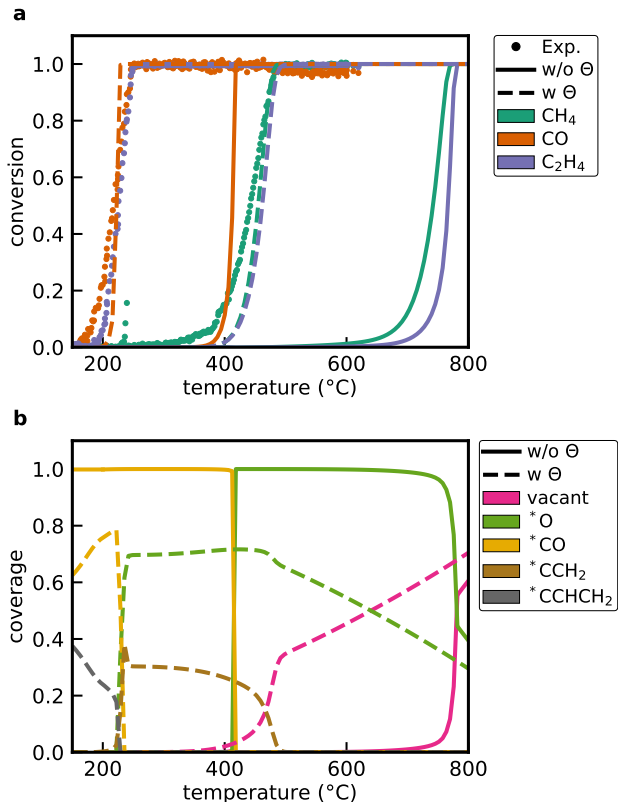
Figure 2: Simulated and experimental a) conversion profiles and b) computed coverages for the oxidation of CO, CH$_4$, and C$_2$H$_4$ (#5). Simulations were performed with (w Θ) and without (w/o Θ) the inclusion of adsorbate-adsorbate interactions.

Adsorbate-adsorbate (or *lateral*) interactions for *CO and *O are strongly repulsive and lead to a destabilization of the adsorbate, which dramatically inhibits the formation of an entire monolayer.[66,78] Therefore, it is necessary to include coverage effects in the microkinetic model. However, at the time of publication, RMG does not include coverage effects in the generation process (though this feature is under active development). Without the inclusion of coverage effects, the reactions are controlled only by the thermochemistry of *CO and *O, since the desorption barrier governs the conversion profile, which corresponds to the heat of formation of the adsorbate. In principle, lateral interactions affect the thermophysical properties of all species as well as the activation energies of all reactions, but computing all these relations with *ab-initio* DFT is not feasible for systems with this degree of complexity. As a simplification, we accounted only for the self-interaction of *O and *CO (see SI). The

inclusion of coverage effects shifts the conversion profile to significantly lower temperatures. CH_4 conversion starts at $400\,°C$ instead of $600\,°C$, while CO is completely converted below $200\,°C$. Surprisingly, CO and CH_4 agree remarkably well with the recorded data, while C_2H_4 shows exactly the same oxidation profile as CH_4, in disagreement with the experiment. The coverage profile also changes drastically, as illustrated in Figure 2b. In addition to $^*O$ and $^*CO$, $^*CCH_2$ as well as $^*CCHCH_2$ cover around a third of the Pt(111) facet. Actually, $^*CCH_2$ shows that C_2H_4 is indeed activated at low temperatures as observed experimentally, but cannot be fully oxidized due to a high barrier in a subsequent elementary step. The reaction path diagram for the C_2H_4 conversion reveals that the adsorption of C_2H_4 results in a physisorbed species, a π-complex. However, the most stable configuration of C_2H_4 on Pt(111) is as a di-σ bidentate adsorbate.[66,79] Although RMG contains bidentate adsorbates in its present database,[30] there are no reaction templates available to manipulate or discover these species (though this, too, is under development). Additionally, the formation of $^*CCHCH_2$ is peculiar, given that the oxidative atmosphere should result in decomposition of C_2H_4 rather than lead to chain growth. The high coverage of this intermediate indicates that it is very stable, which unveils another obstacle: RMG's current thermochemistry database contains only adsorbates with no more than two heavy[30] atoms (with the exception of CO_2^*, $^*COOH$, and $HCOO^*$, which were recently added[80]). Therefore, the thermochemistry of $^*CCHCH_2$ is only estimated via RMG's built-in routines. While all thermochemistry properties of the discovered intermediates for the C_1 chemistry are known, this makes up only a small fraction of the more complex mechanisms, with most intermediates being estimates. Therefore, an important task is to assess the accuracy of RMG's thermochemistry estimates for larger adsorbates, refine these estimates, and to include functionalities for bidentate adsorbates.

Accuracy of RMG's thermochemistry estimate

RMG can estimate the thermochemistry of all unknown adsorbates,[29] which we describe using CH_2CHC^* as an example (see Figure 3a). To estimate the thermochemistry of the adsorbate, RMG first desorbs the molecule and obtains the thermochemistry of the corresponding gas-phase species. In this particular case, the gas-phase precursor is not included in the precompiled databases, and so RMG estimates the thermophysical properties via group additivity.[21] RMG then applies an adsorption correction to compute the thermochemistry of $^*CCHCH_2$ from the gas-phase precursor $\bullet CCHCH_2$.[57] The correction depends on the difference in the enthalpy between the gas-phase molecule and the adsorbate from the current database, organized in a tree structure, which is based on the thermochemistry database developed by Blöndal et al.[30] RMG descends the tree to the node with the most specific representation of this adsorbate, applying wildcards to functional groups of the molecule. In this case, $\bullet CCHCH_2$ is treated as a wildcard, resulting in the adsorbate $R-^*C$, for which the difference in the thermochemistry of gas-phase and adsorbed $^*CH$ is applied. If a gas-phase species can be found in the databases, the only uncertainty in this approach stems from the applied adsorption correction. However, additional uncertainty is introduced if the gas-phase properties are themselves an estimate, as is the case here.[21]

Over the course of the iterative generation procedure, we performed DFT calculations for adsorbates with 3 and more heavy atoms based on the predictions. As a benchmark study,

we compared the estimate with the DFT-based thermochemistry displayed in a histogram in Figure 3b. A full table with all intermediates and a comparison for entropy and heat capacity is provided in Table S13.
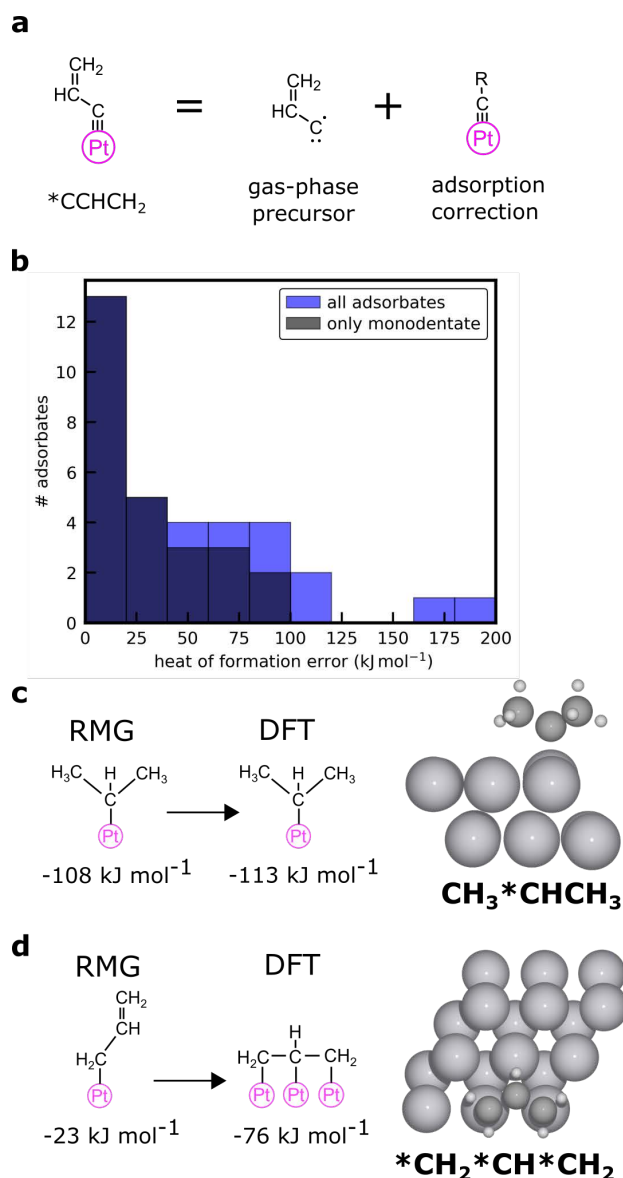
a

*CCHCH$_2$ gas-phase precursor   adsorption correction

b

c

RMG   DFT

-108 kJ mol^{-1} -113 kJ mol^{-1}

CH$_3$*CHCH$_3$

d

RMG   DFT

-23 kJ mol^{-1} -76 kJ mol^{-1}

*CH$_2$*CH*CH$_2$

Figure 3: a) Estimation procedure of the thermochemistry for *CCHCH$_2$. b) Histogram for the error in the estimated heat of formation by RMG for unknown C$_3$ species or C$_1$,C$_2$ oxygenated species and the result from the DFT calculation. c) Predicted and discovered structure for iso-propyl (monodentate adsorbate) and d) for *CH$_2^*$CH*CH$_2$ (tridentate adsorbate) along with the corresponding heats of formation.

The histogram in Figure 3b demonstrates a broad spread in the accuracy of the estimation routine. Most discovered adsorbates have a reasonably accurate estimate of the heat of formation, with a discrepancy to the DFT value below $40 \, \text{kJ} \, \text{mol}^{-1}$ and the mean absolute error (MAE) is $48 \, \text{kJ} \, \text{mol}^{-1}$. The uncertainty of the commonly applied exchange-correlation

functionals such as the BEEF-vdW is on the order of $20\,\mathrm{kJ\,mol^{-1}}$,[50,81,82] so this spread is acceptable. An example adsorbate for a reasonable estimate is provided in Figure 3c. RMG predicts a heat of formation of $-108\,\mathrm{kJ\,mol^{-1}}$ for iso-propyl ($CH_3^*CHCH_3$), and the DFT result is $-113\,\mathrm{kJ\,mol^{-1}}$. Yet, there are some adsorbates for which the heat of formation is off by up to $187\,\mathrm{kJ\,mol^{-1}}$. This error is caused by multiple factors.

First, the accuracy depends mainly on the thermochemistry of the gas-phase precursor. The thermochemistry of most gas-phase adsorbates is based on the ATcT database[54,55] or high-accuracy gas-phase coupled-cluster methods,[83] and is usually known with chemical accuracy (*i.e.* $\pm\,1\,\mathrm{kcal\,mol^{-1}}$). A substantially larger error can be observed if the thermochemical properties of the gas-phase precursor are determined via group additivity. This is quite a challenge for heterogeneous catalysis since some adsorbates, when directly desorbed, would form a species that is at best meta-stable in the gas phase, and therefore no accurate thermochemistry data are available.

Second, RMG predicts the heat of formation based on a monodentate structure for some adsorbates, but subsequent DFT calculations confirmed that the adsorbate is in fact bidentate or tridentate, as illustrated in Figure 3d for $^*CH_2^*CH^*CH_2$. The multidentate adsorbates tend to bind more strongly to the surface. RMG does currently not find the most stable chemical graph representation of the adsorbate, which leads to a wrong adsorption correction.

Lastly, the adsorption corrections are based on a database with small molecules, and there can be a significant change in the thermochemistry from molecules with 1-2 heavy atoms to molecules containing more than 3. For example, the change in thermochemical properties from $^*CH$ to $^*CCH_3$ is probably larger than the change from $^*CCH_2CH_3$ to $^*CCH_2CH_2CH_3$. This phenomenon is reported and exploited in first-principle-based microkinetic modeling studies on the Fischer-Tropsch synthesis.[84] Also, the binding site of the molecule used for the adsorption correction might be different from the most stable binding site determined with DFT. With more thermochemical data of larger molecules becoming available, the present corrections can be refined to provide better estimates for larger molecules. In a worst-case scenario, these errors are compounded, as is seen for CH_3^*COH, which results in an error of $187\,\mathrm{kJ\,mol^{-1}}$.

Another source of error that has not been considered is systematic uncertainties for the gas-phase energies derived from the BEEF-vdW functional, where often correction factors are applied to match heats of reaction from thermochemical tables.[85,86] If the bidentate adsorbates or adsorbates with unavailable gas-phase chemistry are removed, then the MAE reduces to $30\,\mathrm{kJ\,mol^{-1}}$, which demonstrates that the estimation routine of RMG itself is fairly accurate. The MAE in the entropy of the adsorbates amounts to $38\,\mathrm{J\,K^{-1}\,mol^{-1}}$. In conclusion, all estimates have to be taken as approximate since some predicted structures by RMG do not represent the most stable configuration on the potential energy surface, and it is necessary to refine the thermochemistry properties over the course of the mechanism development.[27]

The present work is the first study that employs the pre-trained machine learning potential from the Open Catalyst Project[36] to obtain converged adsorbate configurations as an initial guess for the DFT calculation. In order to assess the accuracy of the MLP prediction, we

computed the single-point energy of the MLP-relaxed structure with DFT and compared it with the fully DFT relaxed energy. The MAE for all 40 of the C_2 and C_3 adsorbate was $12.5\,\mathrm{kJ\,mol^{-1}}$ (see Table S14 and Figure S5), thus highlighting that the GemNet-dT MLP from the OCP is a powerful tool for a fast-but-reliable energy prediction. The largest deviations are caused by $CH_2^*CCH_3$ ($0.6\,\mathrm{eV}$), $^*CHCHCH_3$ ($0.58\,\mathrm{eV}$), and species with an OCO backbone such as CO_2^* ($-0.5\,\mathrm{eV}$) or HCO^*O ($-0.32\,\mathrm{eV}$). The discrepancy for the OCO backbone is presumably caused by the systematic difficulties of the BEEF-vdW functional to accurately predict the energies of these adsorbates[85,86] and not by GemNet-dT MLP.

Construction of the final microkinetic model

After the first round of mechanism generation, the thermochemistry library for Pt(111) was extended by including missing adsorbates. In the next step, it became apparent that many reactions involving bidentate species should be included. Accordingly, we compiled a reaction library to provide potentially missing bidentate elementary reaction steps based upon the hydrogenolysis of ethane on Pt(111) from the work of Salciccioli et al.[79] (see Table S10). Admittedly, this approach does not enable the full predictive power of RMG for bidentate species, but it allows us to improve the mechanism significantly. This inclusion of a reliable sub-mechanism as a "reaction library" to enhance RMG's predictive capabilities is a well-known practice in RMG's gas-phase community.[24,25] This new iteration led once more to new adsorbates in the core and triggered additional DFT calculations. Simulations with this microkinetic model revealed a too strong binding energy of CO_2^*, caused by the BEEF-vdW functional that faces issues to accurately predict the thermochemistry of gas-phase molecules with an OCO backbone.[85,86] Although the approach for the computation of the heat of formation by Blöndal et al.[30] does not depend on the DFT energy of the gas-phase precursor, we applied a correction factor of $+0.41\,\mathrm{eV}$[52,85,86] to the heat of formation of CO_2^*, CO_3^* and HCO_3^* for the 5th iteration to decrease the heat of adsorption. Metrics for the generated mechanism at each stage of this iterative procedure are illustrated in Figure 4.

Figure 4a differentiates the discovered species by their thermochemistry, whether it is an estimate or a direct database hit. For the mechanism generation for the mixture containing CH_4, CO, CO_2, and H_2 (#4), the size is only affected by the inclusion of the bidentate pathways but not by adding additional thermochemistry values for larger adsorbates. This result was expected, since all C_1 hydrocarbons and oxygenates are already in the database. However, this changes for the mixture with C_2H_4 and C_2H_6 (#7), where the size of the mechanism increases with additional thermochemistry data. The trend for the reactions differs and does not show a clear pattern (see Figure 4b). Again the C_1 chemistry remains unchanged. Yet, adding more accurate thermochemistry values can cause reaction pathways that were feasible before to become irrelevant and vice versa. This highlights the tremendous importance of an accurate thermochemistry for gas-phase molecules and adsorbates,[27,87] especially if BEP relations are used to estimate the barriers. While for the C_1 chemistry, the reactions are mostly equally split into abstraction and dissociation, a significant overhead of abstraction reactions prevails for the C_2 chemistry.

The discovered chemistry depends to a large extent on the termination criterion and the `toleranceMoveToCore`. If the value is set too loosely (larger ϵ), a truncation error may be
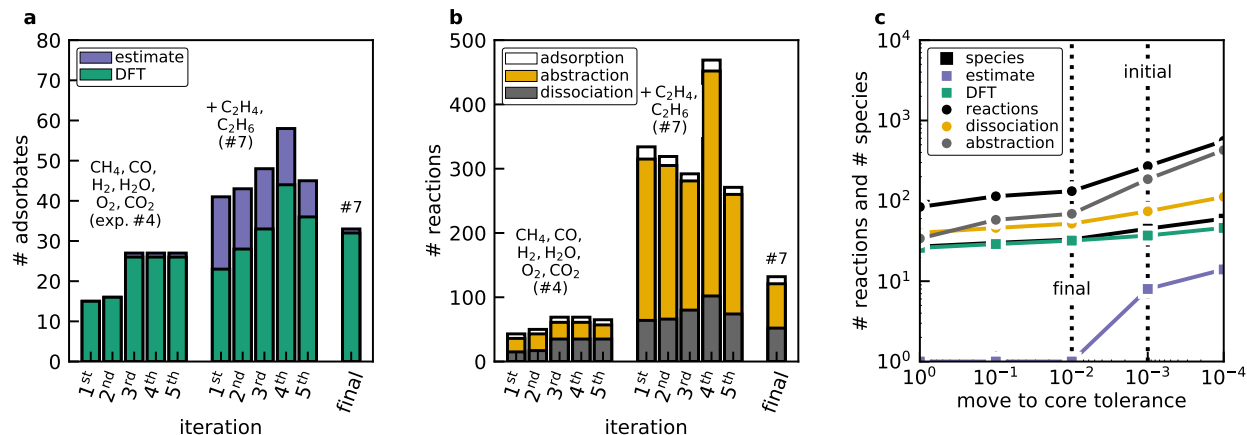
Figure 4: Metrics of the iterative mechanism generation procedure with RMG for the increasing complexity of the gas mixtures. a) Discovered adsorbates; the bar indicates the number of adsorbates that have their thermochemistry based on an estimate from RMG or a DFT-based library value. b) Discovered reactions sorted into the main reaction families, which are adsorption, dissociation, and abstraction. c) Number of adsorbates (squares) and reactions (circles) as a function of RMG's `toleranceMoveToCore` for the mixture containing all gas-phase species (exp. #7). The line is intended to guide the eye. Only reactions and adsorbates from the core are displayed.

included because some important steps might have been missed.[21,29] On the other hand, a too-tight tolerance results in mechanisms containing almost all the possible elementary steps. Such large mechanisms are impractical, because most of the reactions have no significant contribution to the conversion pathways (not to mention numerical issues associated with stiffness). Consequently, the user must ensure that these values are well-chosen, which can be done by generating models for various tolerances and comparing the model predictions in continuum reactor models. We conducted such a convergence study for the C_2 mechanism after the fifth iteration step to determine the required tolerance (see Figure 4c). When mechanisms are generated for a `toleranceMoveToCore` of 1×10^{-2} all discovered adsorbates are based on DFT values, while increasing the value further adds only estimates to the core. Simulations with the microkinetics from the different `toleranceMoveToCore` show that the value can be reduced to 1×10^{-2} without missing important chemistry (see Figure S6), which reduces the computational overhead significantly. The final microkinetic model used for further investigation contains 32 adsorbates, 9 gas-phase species and 132 reactions. In addition to the self-interaction of *O and CO^* discussed before, we added coverage effects for the thermochemistry of $^*CCH_2$ in dependence of the *O and *CO coverage (see SI). Moreover, all reactions which have products that are coverage dependent (*O, *CO, $^*CCH_2$) were rewritten and re-parameterized to make these species the reactants, except the adsorption of CO and O_2. This was done to limit the effect of the coverage-dependent heat of formation on the reaction kinetics for the reversible reactions, explained in depth in the SI.

Evaluation of the generated microkinetic model

Conversion profiles of the final microkinetic model generated by RMG (but the penultimate microkinetic model as described below) and the experiment with all components are shown in Figure 5a. CO conversion sets in at $150\,°C$ in the experiments, whereas the model predicts a value around $200\,°C$. Similarly, the conversion of C_2H_4 is slowed down compared to the experiment. The C_2H_4 conversion follows almost precisely the CO conversion profile, in agreement with the experimental data. Still, the model cannot predict the conversion profiles of both alkanes, while for CH_4 at least the slope is accurately described. In summary, the microkinetics capture the trend in the profiles, except for C_2H_6 and are, thus, in qualitative agreement with the experiments but fail to quantitatively match the recorded data. The generated mechanism was significantly improved through the iterative refinement procedure and the predicted profiles are reasonably close to the experiments. A better agreement can be obtained by adjusting the activation energies of the rate-determining steps within reasonable uncertainty boundaries. This procedure combines the bottom-up approach of first-principles-based mechanism generation with a top-down regression of activation energies.[88,89] DRC analysis was used to identify the most important elementary reactions in the pathways for each species, and the results are displayed in Figures S7 and S8.
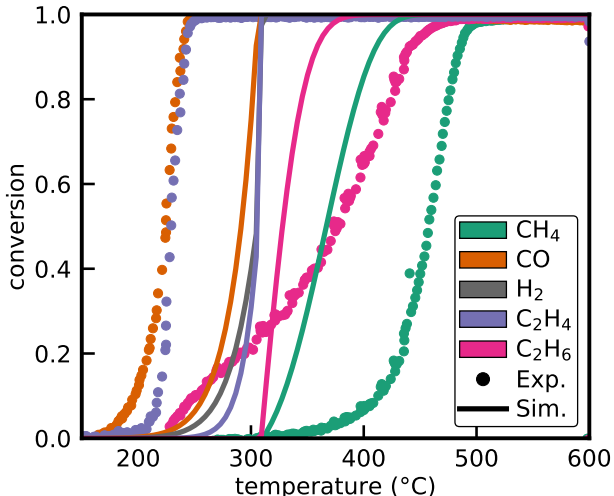

Figure 5: Comparison of the experiments with the final generated microkinetic model by RMG (but the penultimate model as described below) for the complete gas mixture (exp. #7).

The rate-determining step in the CO oxidation pathway is the oxidation of *CO via *CO + *O $\rightleftharpoons$ CO$_2^*$ + * (see Figure S8). Oxidation of CH_4 and C_2H_6 is controlled by the respective dissociative adsorption reactions, CH_4 + 2* $\rightleftharpoons$ *CH$_3$ + H* and C_2H_6 + 2* $\rightleftharpoons$ *CH$_2$CH$_3$ + *H, also demonstrated in numerous earlier studies.[5,6,8,19,90,91] The activation barrier for the CO$_2^*$ formation and the parameters of the Arrhenius expression for the sticking coefficient were fitted to match the experimental results. Parameter regression was performed one parameter at a time using the SciPy package. Barriers for the dehydrogenation of vinyl (*CH*CH$_2$ + * $\rightleftharpoons$ *CH*CH + *H) and the C-C scission of acetylene (*CH*CH $\rightleftharpoons$

$2\,{}^*CH$) have a high degree of rate control for the oxidation of C_2H_4. Consequently, the activation energies for these two reactions were optimized to the experimental data as well. The adjusted parameters are summarized in Table 3. Results from the optimized microkinetic model are reported for all experiments in Figure 6.

Table 3: Reactions that were fitted to the experiment with their initial and final parameters.

reaction	initial		fitted	
	$A\,/\,\mathrm{cm^2\,mol^{-1}\,s^{-1}}$ or $A\,/\,\mathrm{s^{-1\ddagger}}$ or $s\,/\,1^\dagger$	$E_a\,/\,\mathrm{kJ\,mol^{-1}}$	$A\,/\,\mathrm{cm^2\,mol^{-1}\,s^{-1}}$ or $A\,/\,\mathrm{s^{-1\ddagger}}$ or $s\,/\,1^\dagger$	$E_a\,/\,\mathrm{kJ\,mol^{-1}}$
$CH_4 + 2^* \rightleftharpoons {}^*CH_3 + {}^*H$	$6.04^\dagger$	58.0	$12.475^\dagger$	76.2
$C_2H_6 + 2^* \rightleftharpoons {}^*CH_2CH_3 + {}^*H$	$2.052^\dagger$	42.7	$0.866^\dagger$	48.9
${}^*CO + {}^*O \rightleftharpoons CO_2^* + {}^*$	7.27×10^{19}	112.8	7.27×10^{19}	92.7
${}^*CH{}^*CH + {}^*H \rightleftharpoons {}^*CH{}^*CH_2 + {}^*$	4.18×10^{21}	94.6	4.18×10^{21}	86.2
${}^*CH{}^*CH \rightleftharpoons 2\,{}^*CH$	$1.0 \times 10^{13\ddagger}$	124.7	$1.0 \times 10^{13\ddagger}$	107.9

In the case of the CH_4 and CO oxidation (Figure 6a,b), the conversion profiles of the model are shifted to lower temperatures compared to the experiments. However, the model accurately predicts the conversion of CO and C_2H_4 for the more complicated mixtures that contain H_2 (Figure 6c-f). There is only a slight deviation for the CH_4 profile at high temperatures and at low temperatures for C_2H_6. Overall, a good agreement with the experiments can be achieved by minor adjustments of the barriers of the most important elementary steps within their uncertainty range, while the rest of the model is based on first principles and approximate first-principles-based relations (eg. BEP relations).

The discrepancy between the model and experiment for the case of pure CO and CH_4 conversion can be explained by the morphological changes of the Pt crystals. Due to the absence of reductive gases, especially H_2, Pt is more prone to oxidation at lower temperatures, and the available surface area of the more active metallic phase could be reduced.[77] Moreover, the surface coverage and oxidation state of the Pt crystals can change across the packed-bed, as observed in operando experiments for the CO oxidation under lean combustion conditions.[76,77] Under stoichiometric conditions, these changes could be even more facile due to the complete depletion of the reductive gases and O_2 at full conversion. Although, the incorporation of surface oxidation can be done in a somewhat *ad hoc* manner by adjusting the active surface area,[9,73,92] a more rigorous and predictive description can only be achieved with *ab-initio* computations.[93] Figure S11 shows that the microkinetic model can reproduce the experimental results by only adjusting the active surface area. Additionally, the deviation can also be caused by the assumption that only the static Pt(111) facet is the active site, which is a strong simplification of the complex multifaceted Pt crystals on the support that can also transform dynamically during the experiment depending on the local gas atmosphere.[94,95] Avanesian et al.[96] observed a major but still reversible reconstruction of the Pt nanoparticles when they were exposed to a CO atmosphere at elevated pressure. Consequently, we think that the discrepancies between the model and the recorded concentrations for the experiments without H_2 and also for the small deviations for the experiments with H_2 are not caused by missing reaction pathways, but rather are due to the omission of the dynamic and multifaceted nature of the catalyst under reaction conditions, including the
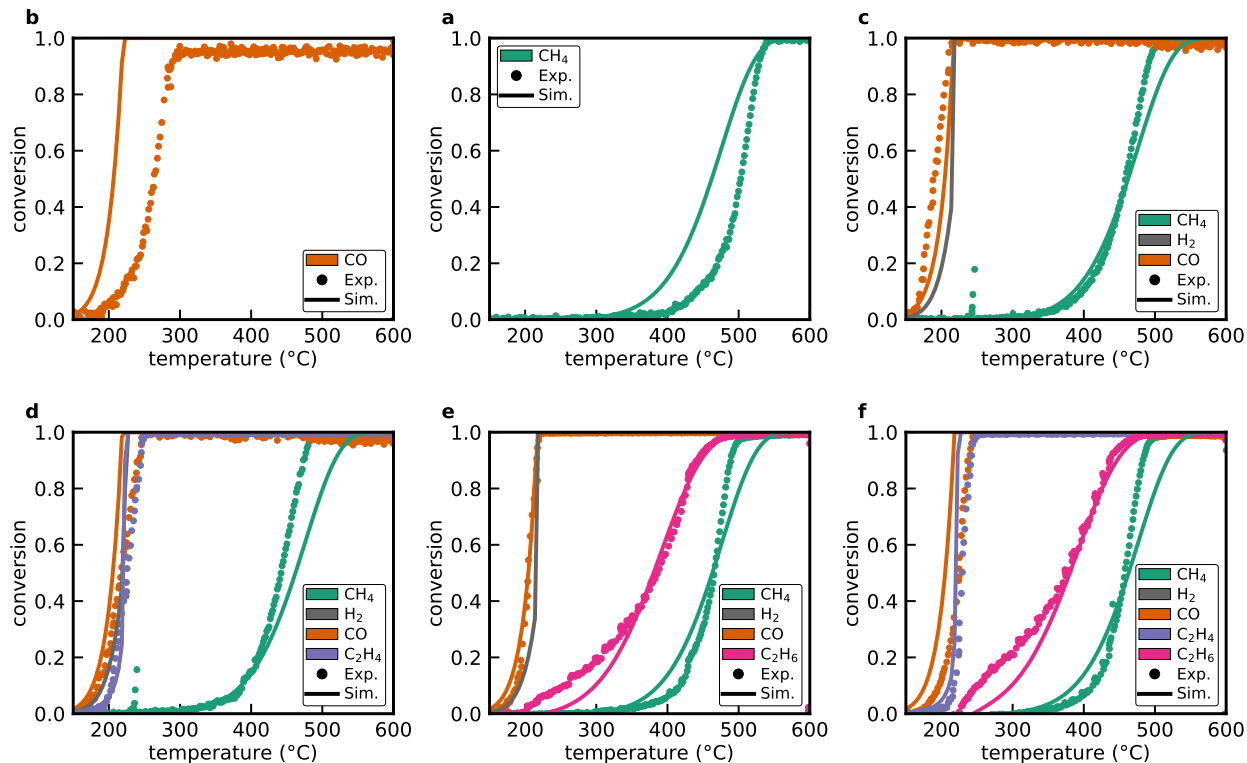
18

Figure 6: Comparison of the final microkinetic model with adjusted activation barriers of the rate-controlling steps with the experiments. a) CO oxidation (#2), b) CH_4 oxidation in CO_2 and H_2O atmosphere (#3), d) +CO and H_2 (#4), e) +C_2H_4 (#5), f) +C_2H_6 (#6), and g) +C_2H_4 +C_2H_6 (#7).

noble metal's oxidation state. Therefore, this study underscores the importance of including morphological changes of the Pt crystals and the support, such as sintering,[73] cluster formation,[95] re-dispersion, and oxidation[76,77,94,97] and surface reconstruction[96] into the microkinetic model and the automated mechanism generation procedure. However, such an integration on a first-principles basis is beyond the scope of the present work.

Figure 7 displays the coverage profile for experiment #7, but this is similar for all cases. A high CO^* coverage is obtained at low temperatures under these stoichiometric conditions in agreement with other studies.[10,77] The surface is covered by O^*, after CO is converted. In addition, there is a small coverage of CH^* at low temperatures, formed by the C-C scission of CH^*-CH^* from ethylene decomposition. The thermodynamic sensitivity analysis shows that CO and C_2H_4 oxidation is sensitive to the heat of formation of CO^*, whereas CH_4 and C_2H_6 are only controlled by the O^* thermochemistry (see Figure S9). This is caused by the coverage on the surface since CO and C_2H_4 are converted at low temperatures, where the the CO^* coverage is high. Additionally, the oxidation of CO^* has a high DRC for both pathways and the thermochemistry affects the rate of oxidation as well as the equilibrium. CH_4 and C_2H_6 are converted at high O^* coverage.

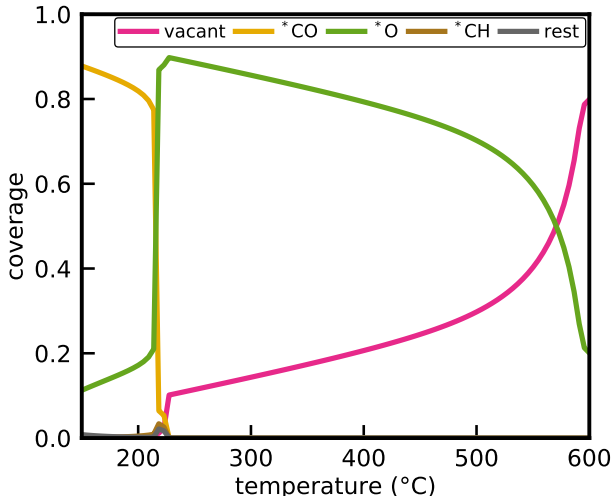A reaction path diagram for the conditions in Figure 5d, namely exp. #7 is displayed in

Figure 7: Simulated coverage profile for the oxidation of the complete mixture from exp. #7 (CH_4, H_2, CO, C_2H_4 and C_2H_6).

Figure 8. CH_4, C_2H_4, and C_2H_6 are converted to *CH through dissociation reactions without the assistance of *O. This observation is also the outcome of most DFT-based mechanism development studies.[98] In contrast, Peela et al.[6] showed that C_2H_6 can also be activated by *O at high coverages via an Eley-Rideal step when the activation barrier was subjected to a coverage-dependence. With the coverage-dependent heat of formation of *O in this study, there is a considerable fraction of vacant sites present at all temperatures, which explains the high reaction rate of C_2H_6 oxidation without the O-assisted pathway. However, the omission of these pathways could contribute to the small deviation between model and experiments at low temperatures, where *O coverage is high. Currently, although RMG can in principle include Eley-Rideal reactions, this reaction family lacks reliable BEP rules and, therefore, was not considered in the mechanism generation procedure.

There are three pathways from *CH to *CO: via formyl (H*CO), hydroxymethylidyne (*COH), and *C, with the first pathway being the main route at all temperatures considered here. Formyl is formed from *CH by direct oxidation according to *CH + *O $\rightleftharpoons$ H*CO + *. A side branch at low temperatures forms formyl from formaldehyde, which itself is produced mostly by oxidative dehydrogenation reactions (see Figure S10). The *COH intermediate is formed via abstraction of the H atom from *CH by *CO: *CH + *CO $\rightleftharpoons$ *COH + *. Carbon formation occurs through direct CH dissociation and by an oxidative dehydrogenation reaction (*CH + *O $\rightleftharpoons$ *C + *OH). A higher temperature increases the fraction of *CO produced through this carbon pathway. Most of the CO_2^* and thence CO_2 is produced by direct oxidation of *CO. Yet, the oxidation to carboxyl (*CO + *OH $\rightleftharpoons$ *COOH + *) and the subsequent oxidative dehydrogenation reaction (*COOH + *O $\rightleftharpoons$ CO_2^* + *OH) contribute to CO_2^* formation as well.

The simulation results demonstrate the importance of coverage-dependent thermochemistry, since it significantly alters the rates, which affects the discovered pathways, especially at low temperatures. Additionally, RMG needs better functionality for multidentate species to
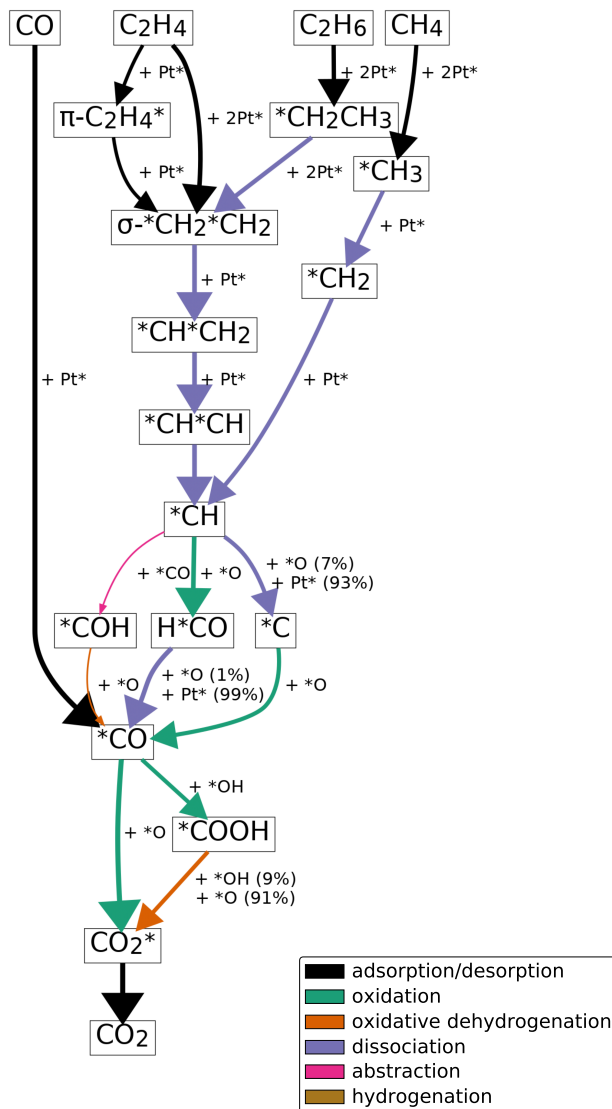
Figure 8: Reaction path diagram following the carbon element for a temperature of 350 °C. The thickness of the arrow illustrates the reaction rate.

discover all the relevant pathways for reactions of larger adsorbates. However, we want to stress that this problem is not unique to automated mechanism generation, and that multi-dentate adsorbates are also challenging to consider during manual mechanism construction due to multiple potential configurations. Thermophysical properties, principally heats of formation, are highly important in microkinetic modeling, whether it is in the gas phase or on the surface.[24,27,87] When BEP relations are employed to estimate the activation barrier of a reaction, the thermochemistry should be as accurate as possible to avoid the propagation of an estimation error into the barrier, which could affect the entire mechanism.

Given that it is relatively inexpensive to perform geometry optimizations, especially in combination with machine learning potentials from the OCP[36] or MLP with active learning[53], the construction of large datasets with thermochemical properties for adsorbates is within

reach at low cost and should receive a high priority for the construction of microkinetics with RMG. The approach outlined in this study produces a first-principles-based microkinetic model that can describe experimental results from a Pt monolith with remarkable accuracy after the 5 elementary reactions with the highest degree of rate control were adjusted within their uncertainties. The model fidelity suggests that Pt(111) could be the active site for the oxidation of these molecules, which is controversially discussed.[5,18,19,91] Larger Pt clusters, which contain a higher fraction of terrace sites, exhibit a higher activity due to the weaker interaction with *O support these findings.[19,91] However, we have to consider the impact of the parametric uncertainty from the DFT-based estimation routines and parameters, which can lead to a broad range of possible solutions.[32,87] To reduce the uncertainty margin further, it is suggested to perform transition state calculations for the most important pathways to refine the microkinetics, where the methodology proposed herein can serve as a hierarchical refinement procedure.[93] Additionally, other facets can and do contribute to the conversion of the pollutants and the entire multifaceted nature of the crystals on the support need to be considered in the microkinetic model.[80,94,95] In principle, RMG can construct microkinetic models for all possible Pt facets if accurate thermochemical tables and BEP relations are provided. Through the usage of RMG within the framework described in the manuscript, the microkinetics for the complex mixture can be constructed in a fraction of the time required to build them manually, and RMG thus streamlines the entire process.

Conclusion

In this study, we have demonstrated how RMG can be applied to aid in the construction of microkinetic models for heterogeneously catalyzed reactions. RMG was used to develop a first-principles-based microkinetic model for the catalytic conversion of stoichiometric exhaust gases from typical gasoline engines on Pt(111). The thermophysical properties of discovered adsorbates were refined at low computational cost by using a machine learning potential from the Open Catalyst Project followed by electronic structure calculations with the BEEF-vdW functional. ML acceleration strategies will be critical to the successful application of RMG to even more complex chemistries and materials as the number of possible adsorbate configurations increases. The approach will also increase in performance as more accurate pre-trained graph potentials are released.[99,100] Activation energies of important elementary reactions were adjusted within confined uncertainty ranges, which resulted in a good agreement with kinetic catalyst tests with a Pt/Al_2O_3 monolith. The comparison of the microkinetic modeling results with the experiments suggest that the catalyst undergoes morphological changes, such as oxidation and reconstruction during the treatment of emissions from stoichiometric combustion conditions depending on the composition of the exhaust gas mixture. This dynamic transformation of the Pt crystals has to be integrated into the microkinetic models on a first-principles basis to accurately describe the conversion of the emissions under the fully transient operating conditions in stoichiometric gasoline direct injection engines. Additionally, the study has also unveiled current limitations in RMG, which were critically discussed. The accuracy and functionalities of RMG are primarily limited by the available data in its databases.

Acknowledgement

Supporting Information Available

Supporting information to this article is available online.

Detailed information on the theoretical methods; DFT raw data; final microkinetic model; additional simulation results.

References

(1) Farrauto, R. J.; Deeba, M.; Alerasool, S. Gasoline automobile catalysis and its historical journey to cleaner air. *Nat. Catal.* **2019**, *2*, 603–613.

(2) Datye, A. K.; Votsmeier, M. Opportunities and challenges in the development of advanced materials for emission control catalysts. *Nat. Mater.* **2021**, *20*, 1049–1059.

(3) Schauer, J. J.; Kleeman, M. J.; Cass, G. R.; Simoneit, B. R. T. Measurement of emissions from air pollution sources. 5. C1-C32 organic compounds from gasoline-powered motor vehicles. *Environ. Sci. Technol.* **2002**, *36*, 1169–1180.

(4) Tanaka, M.; Warashina, M.; Itano, Y.; Tsujimoto, Y.; Wakamatsu, S. Effects of super-light-duty gasoline and LPG-fueled cars on 16 ambient hydrocarbons at roadsides in Japan. *Chemosphere - Global Change Science* **2001**, *3*, 199–207.

(5) Trinchero, A.; Hellman, A.; Grönbeck, H. Methane oxidation over Pd and Pt studied by DFT and kinetic modeling. *Surf. Sci.* **2013**, *616*, 206–213.

(6) Peela, N. R.; Sutton, J. E.; Lee, I. C.; Vlachos, D. G. Microkinetic Modeling of Ethane Total Oxidation on Pt. *Ind. Eng. Chem. Res.* **2014**, *53*, 10051–10058.

(7) Qi, W.; Ran, J.; Wang, R.; Du, X.; Shi, J.; Ran, M. Kinetic mechanism of effects of hydrogen addition on methane catalytic combustion over Pt(111) surface: A DFT study with cluster modeling. *Comput. Mater. Sci.* **2016**, *111*, 430–442.

(8) Chen, Y.; Vlachos, D. G. Density Functional Theory Study of Methane Oxidation and Reforming on Pt(111) and Pt(211). *Ind. Eng. Chem. Res.* **2012**, *22*, 12244–12252.

(9) Chan, D.; Tischer, S.; Heck, J.; Diehm, C.; Deutschmann, O. Correlation between catalytic activity and catalytic surface area of a Pt/Al$_2$O$_3$ DOC: An experimental and microkinetic modeling study. *Appl. Catal., B* **2014**, *156-157*, 153–165.

(10) Koop, J.; Deutschmann, O. Detailed surface reaction mechanism for Pt-catalyzed abatement of automotive exhaust gases. *Appl. Catal., B* **2009**, *91*, 47–58.

(11) Boll, W.; Tischer, S.; Deutschmann, O. Loading and Aging Effects in Exhaust Gas After-Treatment Catalysts with Pt As Active Component. *Ind. Eng. Chem. Res.* **2010**, *49*, 10303–10310.

(12) Mhadeshwar, A. B.; Vlachos, D. G. A Catalytic Reaction Mechanism for Methane Partial Oxidation at Short Contact Times, Reforming, and Combustion, and for Oxygenate Decomposition and Oxidation on Platinum. *Ind. Eng. Chem. Res.* **2007**, *46*, 5310–5324.

(13) Kraus, P.; Lindstedt, R. P. Microkinetic Mechanisms for Partial Oxidation of Methane over Platinum and Rhodium. *J. Phys. Chem. C* **2017**, *121*, 9442–9453.

(14) Aghalayam, P.; Park, Y.; Fernandes, N.; Papavassiliou, V.; Mhadeshwar, A.; Vlachos, D. A C1 mechanism for methane oxidation on platinum. *J. Catal.* **2003**, *213*, 23–38.

(15) Kota, A. S.; Dadi, R. K.; Luss, D.; Balakotaiah, V. Analysis of light-off during oxidation of reactant mixtures on Pt/Al2O3 using micro-kinetic models. *Chem. Eng. Sci.* **2017**, *166*, 320–333.

(16) Psofogiannakis, G.; St-Amant, A.; Ternan, M. Methane oxidation mechanism on Pt(111): a cluster model DFT study. *J. Chem. Phys. B* **2006**, *110*, 24593–24605.

(17) Wang, R.; Chen, J.; Zhao, W.; Wen, J.; Li, H.; Li, L.; Ran, J. Mechanism of the catalytic oxidation of methane on Pt(111) surfaces in moist environment: A density functional theory study. *Appl. Surf. Sci.* **2019**, *471*, 566–586.

(18) Yoo, J. S.; Schumann, J.; Studt, F.; Abild-Pedersen, F.; Nørskov, J. K. Theoretical Investigation of Methane Oxidation on Pd(111) and Other Metallic Surfaces. *J. Phys. Chem. C* **2018**, *122*, 16023–16032.

(19) Chin, Y.-H. C.; Buda, C.; Neurock, M.; Iglesia, E. Reactivity of chemisorbed oxygen atoms and their catalytic consequences during CH$_4$-O$_2$ catalysis on supported Pt clusters. *J. Am. Chem. Soc.* **2011**, *133*, 15958–15978.

(20) Margraf, J. T.; Reuter, K. Systematic Enumeration of Elementary Reaction Steps in Surface Catalysis. *ACS Omega* **2019**, *4*, 3370–3379.

(21) Gao, C. W.; Allen, J. W.; Green, W. H.; West, R. H. Reaction Mechanism Generator: Automatic construction of chemical kinetic mechanisms. *Comput. Phys. Commun.* **2016**, *203*, 212–225.

(22) Liu, M.; Grinberg Dana, A.; Johnson, M. S.; Goldman, M. J.; Jocher, A.; Payne, A. M.; Grambow, C. A.; Han, K.; Yee, N. W.; Mazeau, E. J.; Blondal, K.; West, R. H.; Goldsmith, C. F.; Green, W. H. Reaction Mechanism Generator v3.0: Advances in Automatic Mechanism Generation. *J. Chem. Inf. Model.* **2021**, *61*, 2686–2696.

(23) Green, W. H.; West, R. H. RMG - Reaction Mechanism Generator. `https://rmg.mit.edu/`, 2021; Version 3.0.

(24) Vermeire, F. H.; Aravindakshan, S. U.; Jocher, A.; Liu, M.; Chu, T.-C.; Hawtof, R. E.; van de Vijver, R.; Prendergast, M. B.; van Geem, K. M.; Green, W. H. Detailed Kinetic Modeling for the Pyrolysis of a Jet A Surrogate. *Energy Fuels* **2022**, *45*, 259.

(25) Vandewiele, N. M.; Magoon, G. R.; van Geem, K. M.; Reyniers, M.-F.; Green, W. H.; Marin, G. B. Kinetic Modeling of Jet Propellant-10 Pyrolysis. *Energy Fuels* **2015**, *29*, 413–427.

(26) Harper, M. R.; van Geem, K. M.; Pyl, S. P.; Marin, G. B.; Green, W. H. Comprehensive reaction mechanism for n-butanol pyrolysis and combustion. *Combust. Flame* **2011**, *158*, 16–41.

(27) Pio, G.; Dong, X.; Salzano, E.; Green, W. H. Automatically generated model for light alkene combustion. *Combust. Flame* **2022**, *241*, 112080.

(28) Payne, A. M.; Spiekermann, K. A.; Green, W. H. Detailed Reaction Mechanism for 350–400 °C Pyrolysis of an Alkane, Aromatic, and Long-Chain Alkylaromatic Mixture. *Energy Fuels* **2022**, *36*, 1635–1646.

(29) Goldsmith, C. F.; West, R. H. Automatic Generation of Microkinetic Mechanisms for Heterogeneous Catalysis. *J. Phys. Chem. C* **2017**, *121*, 9970–9981.

(30) Blondal, K.; Jelic, J.; Mazeau, E.; Studt, F.; West, R. H.; Goldsmith, C. F. Computer-Generated Kinetics for Coupled Heterogeneous/Homogeneous Systems: A Case Study in Catalytic Combustion of Methane on Platinum. *Ind. Eng. Chem. Res.* **2019**, *58*, 17682–17691.

(31) Mazeau, E. J.; Satpute, P.; Blöndal, K.; Goldsmith, C. F.; West, R. H. Automated Mechanism Generation Using Linear Scaling Relationships and Sensitivity Analyses Applied to Catalytic Partial Oxidation of Methane. *ACS Catal.* **2021**, *73*, 7114–7125.

(32) Kreitz, B.; Sargsyan, K.; Blöndal, K.; Mazeau, E. J.; West, R. H.; Wehinger, G. D.; Turek, T.; Goldsmith, C. F. Quantifying the Impact of Parametric Uncertainty on Automatic Mechanism Generation for CO_2 Hydrogenation on Ni(111). *JACS Au* **2021**, *1*, 1656–1673.

(33) Abild-Pedersen, F.; Greeley, J.; Studt, F.; Rossmeisl, J.; Munter, T. R.; Moses, P. G.; Skúlason, E.; Bligaard, T.; Nørskov, J. K. Scaling properties of adsorption energies for hydrogen-containing molecules on transition-metal surfaces. *Phys. Rev. Lett.* **2007**, *99*, 016105.

(34) Kreitz, B.; Wehinger, G. D.; Goldsmith, C. F.; Turek, T. In *30th European Symposium on Computer Aided Process Engineering*; Pierucci, S., Manenti, F., Bozzano, G. L., Manca, D., Eds.; Comput.-Aided Chem. Eng.; Elsevier, 2020; Vol. 48; pp 529–534.

(35) Kreitz, B.; Martínez Arias, A.; Martin, J.; Weber, A. P.; Turek, T. Spray-Dried Ni Catalysts with Tailored Properties for CO_2 Methanation. *Catalysts* **2020**, *10*, 1410.

(36) Chanussot, L. *et al.* Open Catalyst 2020 (OC20) Dataset and Community Challenges. *ACS Catal.* **2021**, *11*, 6059–6072.

(37) Karinshak, K. A.; Lott, P.; Harold, M. P.; Deutschmann, O. In situ Activation of Bimetallic Pd-Pt Methane Oxidation Catalysts. *ChemCatChem* **2020**, *12*, 3712–3720.

(38) Karakaya, C.; Deutschmann, O. A simple method for CO chemisorption studies under continuous flow: Adsorption and desorption behavior of Pt/Al_2O_3 catalysts. *Appl. Catal., A* **2012**, *445-446*, 221–230.

(39) Bergeret, G.; Gallezot, P. *Handbook of Heterogeneous Catalysis*; John Wiley & Sons, Ltd, 2008; Chapter 3.1.2, pp 738–765.

(40) Schütz, J.; Störmer, H.; Lott, P.; Deutschmann, O. Effects of Hydrothermal Aging on CO and NO Oxidation Activity over Monometallic and Bimetallic Pt-Pd Catalysts. *Catalysts* **2021**, *11*.

(41) Rappé, K. G.; DiMaggio, C.; Pihl, J. A.; Theis, J. R.; Oh, S. H.; Fisher, G. B.; Parks, J.; Easterling, V. G.; Yang, M.; Stewart, M. L.; Howden, K. C. Aftertreatment Protocols for Catalyst Characterization and Performance Evaluation: Low-Temperature Oxidation, Storage, Three-Way, and NH_3-SCR Catalyst Test Protocols. *Emiss. Control Sci. Technol.* **2019**, *5*, 183–214.

(42) Auckenthaler, T. S.; Onder, C. H.; Geering, H. P. Online Estimation of the Oxygen Storage Level of a Three-Way Catalyst. SAE 2004 World Congress & Exhibition. 2004.

(43) Balenović, M.; Edwards, J.; Backx, T. Vehicle application of model-based catalyst control. *Control Eng. Pract.* **2006**, *14*, 223–233, Advances in Automotive Control (AC'04).

(44) Bickel, J.; Odendall, B.; Eigenberger, G.; Nieken, U. Oxygen storage dominated three-way catalyst modeling for fresh catalysts. *Chem. Eng. Sci.* **2017**, *160*, 34–53.

(45) Gremminger, A.; Pihl, J.; Casapu, M.; Grunwaldt, J.-D.; Toops, T. J.; Deutschmann, O. PGM based catalysts for exhaust-gas after-treatment under typical diesel, gasoline and gas engine conditions with focus on methane and formaldehyde oxidation. *Appl. Catal., B* **2020**, *265*, 118571.

(46) Giannozzi, P. *et al.* QUANTUM ESPRESSO: a modular and open-source software project for quantum simulations of materials. *J. Phys.: Condens. Matter* **2009**, *21*, 395502.

(47) Giannozzi, P. *et al.* Advanced capabilities for materials modelling with Quantum ESPRESSO. *J. Phys.: Condens. Matter* **2017**, *29*, 465901.

(48) Dal Corso, A. Pseudopotentials periodic table: From H to Pu. *Comput. Mater. Sci.* **2014**, *95*, 337–350.

(49) Larsen, A. H. *et al.* The Atomic Simulation Environment-a Python Library for Working with Atoms. *J. Phys.: Condens. Matter* **2017**, *29*, 273002.

(50) Wellendorff, J.; Lundgaard, K. T.; Møgelhøj, A.; Petzold, V.; Landis, D. D.; Nørskov, J. K.; Bligaard, T.; Jacobsen, K. W. Density functionals for Surf. Sci.: Exchange-correlation model development with Bayesian error estimation. *Phys. Rev. B* **2012**, *85*, 316.

(51) Kittel, C. *Introduction to Solid State Physics*, 8th ed.; Wiley: Hoboken, NJ, 2005.

(52) Streibel, V.; Aljama, H. A.; Yang, A.-C.; Choksi, T. S.; Sánchez-Carrera, R. S.; Schäfer, A.; Li, Y.; Cargnello, M.; Abild-Pedersen, F. Microkinetic Modeling of Propene Combustion on a Stepped, Metallic Palladium Surface and the Importance of Oxygen Coverage. *ACS Catal.* **2022**, *12*, 1742–1757.

(53) Musielewicz, J.; Wang, X.; Tian, T.; Ulissi, Z. FINETUNA: Fine-tuning Accelerated Molecular Simulations. 2022; `https://arxiv.org/abs/2205.01223`.

(54) Ruscic, B.; Bross, D. H. `https://atct.anl.gov`, Active Thermochemical Tables (ATcT) Values Based on ver. 1.122g of the Thermochemical Network.

(55) Ruscic, B.; Pinzon, R. E.; Morton, M. L.; von Laszevski, G.; Bittner, S. J.; Nijsure, S. G.; Amin, K. A.; Minkoff, M.; Wagner, A. F. Introduction to Active Thermochemical Tables: Several "Key" Enthalpies of Formation Revisited. *J. Phys. Chem. A* **2004**, *108*, 9979–9997.

(56) Susnow, R. G.; Dean, A. M.; Green, W. H.; Peczak, P.; Broadbelt, L. J. Rate-Based Construction of Kinetic Models for Complex Systems. *J. Phys. Chem. A* **1997**, *101*, 3731–3740.

(57) Goldsmith, C. F. Estimating the Thermochemistry of Adsorbates Based Upon Gas-Phase Properties. *Top. Catal.* **2012**, *55*, 366–375.

(58) van Santen, R. A.; Neurock, M.; Shetty, S. G. Reactivity theory of transition-metal surfaces: a Brønsted-Evans-Polanyi linear activation energy-free-energy analysis. *Chem. Rev.* **2010**, *110*, 2005–2048.

(59) Sutton, J. E.; Vlachos, D. G. Building large microkinetic models with first-principles accuracy at reduced computational cost. *Chem. Eng. Sci.* **2015**, *121*, 190–199.

(60) Sutton, J. E.; Vlachos, D. G. Effect of errors in linear scaling relations and Brønsted–Evans–Polanyi relations on activity and selectivity maps. *J. Catal.* **2016**, *338*, 273–283.

(61) Jones, G.; Jakobsen, J. G.; Shim, S. S.; Kleis, J.; Andersson, M. P.; Rossmeisl, J.; Abild-Pedersen, F.; Bligaard, T.; Helveg, S.; Hinnemann, B.; Rostrup-Nielsen, J. R.; Chorkendorff, I.; Sehested, J.; Nørskov, J. K. First principles calculations and experimental insight into methane steam reforming over transition metal catalysts. *J. Catal.* **2008**, *259*, 147–160.

(62) Sutton, J. E.; Vlachos, D. G. A Theoretical and Computational Analysis of Linear Free Energy Relations for the Estimation of Activation Energies. *ACS Catal.* **2012**, *2*, 1624–1634.

(63) Sutton, J. E.; Vlachos, D. G. Ethanol Activation on Closed-Packed Surfaces. *Ind. Eng. Chem. Res.* **2015**, *54*, 4213–4225.

(64) Sutton, J. E.; Panagiotopoulou, P.; Verykios, X. E.; Vlachos, D. G. Combined DFT, Microkinetic, and Experimental Study of Ethanol Steam Reforming on Pt. *J. Phys. Chem. C* **2013**, *117*, 4691–4706.

(65) Cushing, G. W.; Navin, J. K.; Donald, S. B.; Valadez, L.; Johánek, V.; Harrison, I. C−H Bond Activation of Light Alkanes on Pt(111): Dissociative Sticking Coefficients, Evans−Polanyi Relation, and Gas−Surface Energy Transfer. *J. Phys. Chem. C* **2010**, *114*, 17222–17232.

(66) W. A. Brown,; R. Kose,; D. A. King, Femtomole Adsorption Calorimetry on Single-Crystal Surfaces. *Chem. Rev.* **1998**, *98*, 797–832.

(67) Wang, S. *et al.* Universal transition state scaling relations for (de)hydrogenation over transition metals. *Phys. Chem. Chem. Phys.* **2011**, *13*, 20760–20765.

(68) Kreitz, B.; Lott, P.; Bae, J.; Blöndal, K.; Angeli, S.; Ulissi, Z. W.; Studt, F.; Goldsmith, C. F.; Deutschmann, O. Data for Detailed microkinetics for the oxidation of exhaust gas emissions through automated mechanism generation. 2022; https://doi.org/10.5281/zenodo.6801552.

(69) Goodwin, D. G.; Speth, R. L.; Moffat, H. K.; Weber, B. W. Cantera: An Object-Oriented Software Toolkit for Chemical Kinetics, Thermodynamics, and Transport Processes. https://www.cantera.org, 2018; Version 2.4.0.

(70) Campbell, C. T. Finding the Rate-Determining Step in a Mechanism. *J. Catal.* **2001**, *204*, 520–524.

(71) Stegelmann, C.; Andreasen, A.; Campbell, C. T. Degree of Rate Control: How Much the Energies of Intermediates and Transition States Control Rates. *J. Am. Chem. Soc.* **2009**, *131*, 8077–8082.

(72) Campbell, C. T. The Degree of Rate Control: A Powerful Tool for Catalysis Research. *ACS Catal.* **2017**, *7*, 2770–2779.

(73) Keller, K.; Lott, P.; Stotz, H.; Maier, L.; Deutschmann, O. Microkinetic Modeling of the Oxidation of Methane Over PdO Catalysts—Towards a Better Understanding of the Water Inhibition Effect. *Catalysts* **2020**, *10*, 922.

(74) Lott, P.; Dolcet, P.; Casapu, M.; Grunwaldt, J.-D.; Deutschmann, O. The Effect of Prereduction on the Performance of Pd/Al_2O_3 and Pd/CeO_2 Catalysts during Methane Oxidation. *Ind. Eng. Chem. Res.* **2019**, *58*, 12561–12570.

(75) Gänzler, A. M.; Casapu, M.; Vernoux, P.; Loridant, S.; Cadete Santos Aires, F. J.; Epicier, T.; Betz, B.; Hoyer, R.; Grunwaldt, J.-D. Tuning the Structure of Platinum Particles on Ceria In Situ for Enhancing the Catalytic Performance of Exhaust Gas Catalysts. *Angew. Chem. Int. Ed.* **2017**, *56*, 13078–13082.

(76) Maurer, F.; Gänzler, A.; Lott, P.; Betz, B.; Votsmeier, M.; Loridant, S.; Vernoux, P.; Murzin, V.; Bornmann, B.; Frahm, R.; Deutschmann, O.; Casapu, M.; Grunwaldt, J.-D. Spatiotemporal Investigation of the Temperature and Structure of a Pt/CeO_2 Oxidation Catalyst for CO and Hydrocarbon Oxidation during Pulse Activation. *Ind. Eng. Chem. Res.* **2021**, *60*, 6662–6675.

(77) Gänzler, A. M.; Casapu, M.; Doronkin, D. E.; Maurer, F.; Lott, P.; Glatzel, P.; Votsmeier, M.; Deutschmann, O.; Grunwaldt, J.-D. Unravelling the Different Reaction Pathways for Low Temperature CO Oxidation on Pt/CeO_2 and Pt/Al_2O_3 by Spatially Resolved Structure-Activity Correlations. *J.Phys. Chem. Lett.* **2019**, *10*, 7698–7705.

(78) Grabow, L. C.; Hvolbæk, B.; Nørskov, J. K. Understanding Trends in Catalytic Activity: The Effect of Adsorbate–Adsorbate Interactions for CO Oxidation Over Transition Metals. *Top. Catal.* **2010**, *53*, 298–310.

(79) Salciccioli, M.; Chen, Y.; Vlachos, D. G. Microkinetic Modeling and Reduced Rate Expressions of Ethylene Hydrogenation and Ethane Hydrogenolysis on Platinum. *Ind. Eng. Chem. Res.* **2011**, *50*, 28–40.

(80) Kreitz, B.; Wehinger, G. D.; Goldsmith, C. F.; Turek, T. Microkinetic Modeling of the CO_2 Desorption from Supported Multifaceted Ni Catalysts. *J. Phys. Chem. C* **2021**, *125*, 2984–3000.

(81) Medford, A. J.; Wellendorff, J.; Vojvodic, A.; Studt, F.; Abild-Pedersen, F.; Jacobsen, K. W.; Bligaard, T.; Nørskov, J. K. Catalysis. Assessing the reliability of calculated catalytic ammonia synthesis rates. *Science* **2014**, *345*, 197–200.

(82) Mallikarjun Sharada, S.; Bligaard, T.; Luntz, A. C.; Kroes, G.-J.; Nørskov, J. K. SBH10: A Benchmark Database of Barrier Heights on Transition Metal Surfaces. *J. Phys. Chem. C* **2017**, *121*, 19807–19815.

(83) Klippenstein, S. J.; Harding, L. B.; Ruscic, B. Ab Initio Computations and Active Thermochemical Tables Hand in Hand: Heats of Formation of Core Combustion Species. *J. Phys. Chem. A* **2017**, *121*, 6580–6602.

(84) Zijlstra, B.; Broos, R. J. P.; Chen, W.; Bezemer, G. L.; Filot, I. A. W.; Hensen, E. J. M. The Vital Role of Step-Edge Sites for Both CO Activation and Chain Growth on Cobalt Fischer–Tropsch Catalysts Revealed through First-Principles-Based Microkinetic Modeling Including Lateral Interactions. *ACS Catal.* **2020**, *10*, 9376–9400.

(85) Peterson, A. A.; Abild-Pedersen, F.; Studt, F.; Rossmeisl, J.; Nørskov, J. K. How copper catalyzes the electroreduction of carbon dioxide into hydrocarbon fuels. *Energy Environ. Sci.* **2010**, *3*, 1311.

(86) Studt, F.; Abild-Pedersen, F.; Varley, J. B.; Nørskov, J. K. CO and CO_2 Hydrogenation to Methanol Calculated Using the BEEF-vdW Functional. *Catal. Lett.* **2013**, *143*, 71–73.

(87) Sutton, J. E.; Guo, W.; Katsoulakis, M. A.; Vlachos, D. G. Effects of correlated parameters and uncertainty in electronic-structure-based chemical kinetic modelling. *Nat. Chem.* **2016**, *8*, 331–337.

(88) Medford, A. J.; Kunz, M. R.; Ewing, S. M.; Borders, T.; Fushimi, R. Extracting Knowledge from Data through Catalysis Informatics. *ACS Catal.* **2018**, *8*, 7403–7429.

(89) Bhandari, S.; Rangarajan, S.; Mavrikakis, M. Combining Computational Modeling with Reaction Kinetics Experiments for Elucidating the In Situ Nature of the Active Site in Catalysis. *Acc. Chem. Res.* **2020**, *53*, 1893–1904.

(90) Zerkle, D. K.; Allendorf, M. D.; Wolf, M.; Deutschmann, O. Understanding Homogeneous and Heterogeneous Contributions to the Platinum-Catalyzed Partial Oxidation of Ethane in a Short-Contact-Time Reactor. *J. Catal.* **2000**, *196*, 18–39.

(91) García-Diéguez, M.; Chin, Y.-H.; Iglesia, E. Catalytic reactions of dioxygen with ethane and methane on platinum clusters: Mechanistic connections, site requirements, and consequences of chemisorbed oxygen. *J. Catal.* **2012**, *285*, 260–272.

(92) Korup, O.; Goldsmith, C. F.; Weinberg, G.; Geske, M.; Kandemir, T.; Schlögl, R.; Horn, R. Catalytic partial oxidation of methane on platinum investigated by spatial reactor profiles, spatially resolved spectroscopy, and microkinetic modeling. *J. Catal.* **2013**, *297*, 1–16.

(93) Wehinger, G. D. *et al.* Quo vadis multiscale modeling in reaction engineering? – A perspective. *Chem. Eng. Res. Des.* **2022**,

(94) Maurer, F.; Jelic, J.; Wang, J.; Gänzler, A.; Dolcet, P.; Wöll, C.; Wang, Y.; Studt, F.; Casapu, M.; Grunwaldt, J.-D. Tracking the formation, fate and consequence for catalytic activity of Pt single sites on CeO_2. *Nat. Catal.* **2020**, *3*, 824–833.

(95) Maurer, F.; Beck, A.; Jelic, J.; Wang, W.; Mangold, S.; Stehle, M.; Wang, D.; Dolcet, P.; Gänzler, A. M.; Kübel, C.; Studt, F.; Casapu, M.; Grunwaldt, J.-D. Surface Noble Metal Concentration on Ceria as a Key Descriptor for Efficient Catalytic CO Oxidation. *ACS Catal.* **2022**, *12*, 2473–2486.

(96) Avanesian, T.; Dai, S.; Kale, M. J.; Graham, G. W.; Pan, X.; Christopher, P. Quantitative and Atomic-Scale View of CO-Induced Pt Nanoparticle Surface Reconstruction at Saturation Coverage via DFT Calculations Coupled with in Situ TEM and IR. *J. Am. Chem. Soc.* **2017**, *139*, 4551–4558.

(97) Carlsson, P.-A.; Fridell, E.; Skoglundh, M. Methane oxidation over Pt/Al_2O_3 and Pd/Al_2O_3 catalysts under transient conditions. *Catal. Lett.* **2007**, *115*.

(98) Yoo, J. S.; Khan, T. S.; Abild-Pedersen, F.; Nørskov, J. K.; Studt, F. On the role of the surface oxygen species during A-H (A = C, N, O) bond activation: a density functional theory study. *Chem. Commun.* **2015**, *51*, 2621–2624.

(99) Zitnick, C. L.; Das, A.; Kolluru, A.; Lan, J.; Shuaibi, M.; Sriram, A.; Ulissi, Z.; Wood, B. Spherical Channels for Modeling Atomic Interactions. *arXiv e-prints* **2022**, arXiv–2206.

(100) Gasteiger, J.; Shuaibi, M.; Sriram, A.; Günnemann, S.; Ulissi, Z.; Zitnick, C. L.; Das, A. How Do Graph Networks Generalize to Large and Diverse Molecular Systems? *arXiv preprint arXiv:2204.02782* **2022**,

Graphical TOC Entry